AD-A166 851 ANALYSIS OF A DOUBLY COUPLED SINGLE FIBER RESONATOR(U) 1/1
AIR FORCE INST OF TECH WRIGHT-PATTERSON AFB OH
R L GLOVER DEC 85 AFIT/CI/NR-86-52T

UNCLASSIFIED F/G 17/7 NL

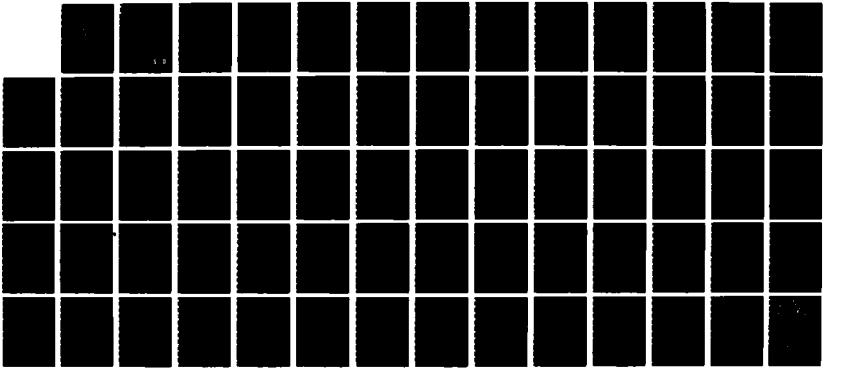

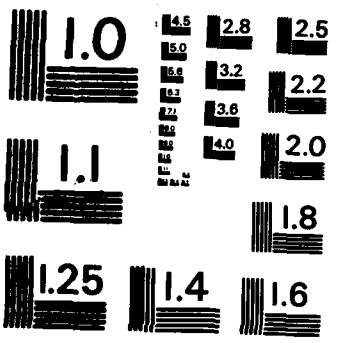

SECURITY CLASSIFICATION OF THIS PAGE *(When Data Entered)*

REPORT DOCUMENTATION PAGE		READ INSTRUCTIONS BEFORE COMPLETING FORM
1. REPORT NUMBER AFIT/CI/NR 86-52T	2. GOVT ACCESSION NO.	3. RECIPIENT'S CATALOG NUMBER
4. TITLE *(and Subtitle)* Analysis of a Doubly Coupled Single Fiber Resonator		5. TYPE OF REPORT & PERIOD COVERED THESIS/DISSERTATION 6. PERFORMING ORG. REPORT NUMBER
7. AUTHOR(s) Richard Lee Glover		8. CONTRACT OR GRANT NUMBER(s)
9. PERFORMING ORGANIZATION NAME AND ADDRESS AFIT STUDENT AT: The University of Texas at Austin		10. PROGRAM ELEMENT, PROJECT, TASK AREA & WORK UNIT NUMBERS
11. CONTROLLING OFFICE NAME AND ADDRESS AFIT/NR WPAFB OH 45433-6583		12. REPORT DATE 1985 13. NUMBER OF PAGES 64
14. MONITORING AGENCY NAME & ADDRESS(if different from Controlling Office)		15. SECURITY CLASS. (of this report) UNCLASS 15a. DECLASSIFICATION/DOWNGRADING SCHEDULE

16. DISTRIBUTION STATEMENT *(of this Report)*

APPROVED FOR PUBLIC RELEASE; DISTRIBUTION UNLIMITED

17. DISTRIBUTION STATEMENT *(of the abstract entered in Block 20, if different from Report)*

18. SUPPLEMENTARY NOTES

APPROVED FOR PUBLIC RELEASE: IAW AFR 190-1

LYNN E. WOLAVER
Dean for Research and Professional Development
AFIT/NR, WPAFB OH 45433-6583
14 April 86

19. KEY WORDS *(Continue on reverse side if necessary and identify by block number)*

20. ABSTRACT *(Continue on reverse side if necessary and identify by block number)*

DTIC ELECTE APR 22 1986 S D A

DD FORM 1 JAN 73 1473 EDITION OF 1 NOV 65 IS OBSOLETE

SECURITY CLASSIFICATION OF THIS PAGE (When Data Entered)

AD-A166 851

DTIC FILE COPY

ABSTRACT

An analysis of a doubly coupled single fiber resonator has been made. The addition of a second coupler to a typical single coupler resonator with less than 100 percent coupling is shown to greatly improve the finesse and sensitivity to fiber attenuation of the resonator. A simple method of achieving extremely high finesse with approximately 70 percent coupling is also shown. With typical fiber and coupler loss values from the literature included in the calculations, this device shows a minimum detectable signal on the order of 20 picometers as a microbend sensor and .17 microradians per second as a laser gyroscope.

ANALYSIS OF A DOUBLY COUPLED SINGLE FIBER RESONATOR

BY

RICHARD LEE GLOVER, BSEE
1LT, USAF

64 pages

THESIS

Presented to the Faculty of the Graduate School of

The University of Texas at Austin

in Partial Fulfillment

of the Requirements

for the Degree of

MASTER OF SCIENCE IN ENGINEERING

THE UNIVERSITY OF TEXAS AT AUSTIN

December 1985

VITA

Richard Lee Glover was born at a U.S. Army hospital on November 27, 1959 in Fountainbleu, France. His parents are William and Kitty Glover. Upon graduation from Parkland High School, El Paso, Texas, he attended West Texas State University and the University of Texas at El Paso (UTEP). After receiving an AFROTC scholarship he graduated from UTEP with a Bachelor of Science in Electrical Engineering in May, 1982.

He was married on May 22, 1982 and was commissioned as an officer in the U.S. Air Force shortly thereafter. After attending Communication Electronics school at Keesler AFB, MS, he was assigned as a Satellite Systems Engineer at Scott AFB, IL, where he served until August 1984. He has been enrolled in the Graduate School at the University of Texas at Austin since that time. His major research area is integrated optics and his minor area of interest is orbital mechanics.

Permanent address: 6016 Redstone Lane
El Paso, Texas 79924.

This thesis was typed by Millie's Typing Services.

ANALYSIS OF A DOUBLY COUPLED SINGLE FIBER RESONATOR

Approved by:

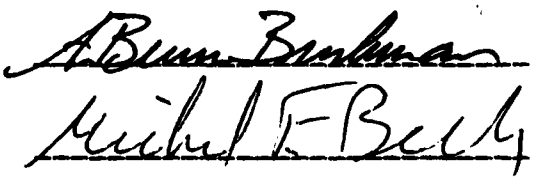

ANALYSIS OF A DOUBLY COUPLED SINGLE FIBER RESONATOR

BY

RICHARD LEE GLOVER, BSEE

THESIS

Presented to the Faculty of the Graduate School of

The University of Texas at Austin

in Partial Fulfillment

of the Requirements

for the Degree of

MASTER OF SCIENCE IN ENGINEERING

THE UNIVERSITY OF TEXAS AT AUSTIN

December 1985

ACKNOWLEDGEMENTS

The author wishes to thank Dr. A. B. Buckman for his assistance and patient guidance during this analysis. The assistance of Dr. M. F. Becker is also greatly appreciated. A sincere appreciation is given to the U.S. Air Force for allowing me the opportunity to pursue my studies. Finally, a special thanks to my wife, Kathy, and son, Richard, without whose love and understanding none of this could have been accomplished.

November 22, 1985

ABSTRACT

An analysis of a doubly coupled single fiber resonator has been made. The addition of a second coupler to a typical single coupler resonator with less than 100 percent coupling is shown to greatly improve the finesse and sensitivity to fiber attenuation of the resonator. A simple method of achieving extremely high finesse with approximately 70 percent coupling is also shown. With typical fiber and coupler loss values from the literature included in the calculations, this device shows a minimum detectable signal on the order of 20 picometers as a microbend sensor and .17 microradians per second as a laser gyroscope.

TABLE OF CONTENTS

LIST OF TABLES

LIST OF FIGURES

LIST OF FIGURES (Continued)

I. INTRODUCTION

The use of evanescent wave coupling in optical fibers allows for the design and implementation of elaborate feedback networks. Since reflections do not occur at the coupling interface, the analysis of these devices is quite straightforward and leads to some very useful results.

One of the dominant applications of fiber optic technology is in the sensor research area. Most fiber optic sensors can be divided into two broad categories: those that employ an amplitude modulation mechanism for detection and those that employ a phase modulation mechanism [3]. Application of these mechanisms to sensor devices include interferometric acoustic sensors [2], fiber microbend acoustic sensors [18], fiber optic accelerometers [19], magnetic field sensors [20], and fiber optic gyroscopes [14, 15]. Another rapidly growing application area is signal processing [12], specifically the use of fibers to form a recirculating delay line [10] and the use of an evanescently coupled feedback network to perform matrix multiplication [11].

The purpose of this thesis is to analyze a particular resonant feedback structure and describe its unique characteristics. Application of this device as a microbend sensor will be discussed in detail and suggestions made for other applications.

II. SIMILAR STRUCTURES

In general, resonators are extremely sensitive to losses in the feedback path. Since low loss fiber is readily available, the key component in the development of a high finesse fiber optic resonator is a low loss coupler. In reference [6], a mechanical lapping technique for the fabrication of a single-mode fiber optic directional coupler was introduced. The coupling in this device was tunable and achieved a power transfer of 70 percent with less than 10 percent loss. When this coupler was first used in an all-single-mode fiber resonator [8], a finesse of 80 was achieved. The dominant loss in this structure was the coupler insertion loss, approximately 3.2 percent.

In ref. [7], a refined mechanical lapping technique was used to fabricate a low loss coupler. This tunable device coupled up to 99.8 percent of the input power with losses approaching .1 percent. In addition,

the authors found that the scattering loss varied with the coupled power. This low loss coupler was used to construct a low loss fiber ring resonator [9]. For a one meter loop loss of .41 percent, the authors measured a finesse of approximately 500 with a coupler loss of .22 percent. Therefore, for the first time, the resonator loss was dominated by the fiber loss rather than the coupler loss.

The development of these low loss fiber resonators will open the door to a whole new family of sensors and optical processing devices. These published results will be applied to the derivations in the applications section. This will allow for a realistic simulation of the device's operation.

III. GENERAL DEVICE DESCRIPTION

The main feedback structure of this device can be constructed from a single length of optical fiber. A general diagram is shown in Figure 1. The supplemental paths A and B can be implemented by using separate lengths of fiber or placing a loop in the main fiber. Note that this design reduces to a simple resonator, described in Section II, when there is zerc coupling at CP1 and the supplemental paths are removed.

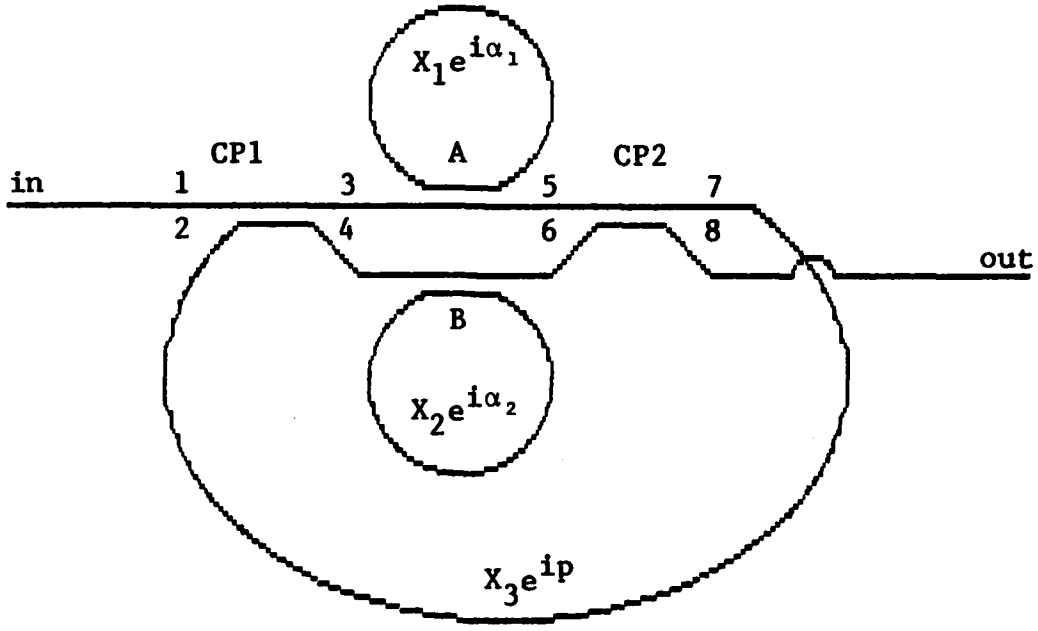

Figure 1: General Diagram of the Double Coupler Device

Using coupled mode theory [1], the evanescent wave coupling that occurs at couplers one and two, CP1 and CP2 respectively, can be described by the following equations:

$$E_3 = t_1E_1 + ir_1E_2 \quad (1)$$

$$E_4 = ir_1E_1 + t_1E_2 \quad (2)$$

$$E_7 = t_2E_5 + ir_2E_6 \quad (3)$$

$$E_8 = ir_2E_5 + t_2E_6 \quad (4)$$

$$r^2 + t^2 + \gamma = 1 \quad (5)$$

where: r^2 = coupled power

t^2 = through put power

γ = coupler power loss

The feedback loop and supplemental paths provide the following additional relationships:

$$E_5 = X_1e^{i\alpha_1}E_3 \quad (6)$$

$$E_6 = X_2e^{i\alpha_2}E_4 \quad (7)$$

$$E_2 = X_3e^{ip}E_7 \quad (8)$$

where: X_1 = transmission coefficient of path A

α_1 = phase shift in path A

X_2 = transmission coefficient of path B

α_2 = phase shift in path B

X_3 = transmission coefficient of feedback loop

p = phase shift in feedback loop

Using equations 1-8, we can determine the value at any port with respect to the input. These values are determined by the following equations:

NOTE: these equations assume that r and t satisfy equation 5.

$$d = 1 - X_1X_3r_1t_2e^{i(p+\alpha_1+\pi/2)} - X_2X_3r_2t_1e^{i(p+\alpha_2+\pi/2)} \quad (9)$$

$$E_2 = \frac{1}{d}\left(X_1X_3t_1t_2e^{i(p+\alpha_1)} - X_2X_3r_1r_2e^{i(p+\alpha_2)}\right)E_1 \quad (10)$$

$$E_3 = \frac{1}{d}\left(t_1 - X_2X_3r_1r_2e^{i(p+\alpha_2+\pi/2)}\right) E_1 \quad (11)$$

$$E_4 = \frac{1}{d}\left(r_1e^{i\pi/2} + X_1X_3t_2e^{i(p+\alpha_1)}\right) E_1 \quad (12)$$

$$E_5 = \frac{1}{d}\left(X_1t_1e^{i\alpha_1} - X_1X_2X_3r_2e^{i(p+\alpha_1+\alpha_2+\pi/2)}\right) E_1 \quad (13)$$

$$E_6 = \frac{1}{d}\left(X_2r_1e^{i(\alpha_2+\pi/2)} + X_1X_2X_3t_2e^{i(p+\alpha_1+\alpha_2)}\right) E_1 \quad (14)$$

$$E_7 = \frac{1}{d}\left(X_1t_1t_2e^{i\alpha_1} - X_2r_1r_2e^{i\alpha_2}\right) E_1 \quad (15)$$

$$E_8 = \frac{1}{d}\left(X_1t_1r_2e^{i(\alpha_1+\pi/2)} + X_2r_1t_2e^{i(\alpha_2+\pi/2)} + X_1X_2X_3e^{i(p+\alpha_1+\alpha_2)}\right) E_1 \quad (16)$$

We can use equation (16) to describe the overall characteristics of the device. We will define the transmittance of the device by:

$$T = \left| \frac{E_8}{E_1} \right|^2 \tag{17}$$

and the net optical phase shift by:

$$\Phi = \tan^{-1} \left| \frac{\mathrm{Im}(E_8/E_1)}{\mathrm{Re}(E_8/E_1)} \right| \tag{18}$$

IV. SUPPLEMENTAL PATH DESIGN

Two simple methods for implementing the supplemental paths are shown in Figures 2 and 3. The method of Figure 2 could be used when a more sensitive fiber is required in order to detect changes in Z or α_z. The transmission coefficient and phase for this method is described by the following equation:

$$\frac{E_3}{E_1} = \frac{t - Ze^{i\alpha_z}}{1 - tZe^{i\alpha_z}} \tag{19}$$

For the case of very strong coupling, t = 0, the transmission coefficient and phase are completely determined by the loop characteristics:

$$\frac{E_3}{E_1} \quad -Ze^{i\alpha_z} = Ze^{i(\alpha_z + \pi)} \tag{20}$$

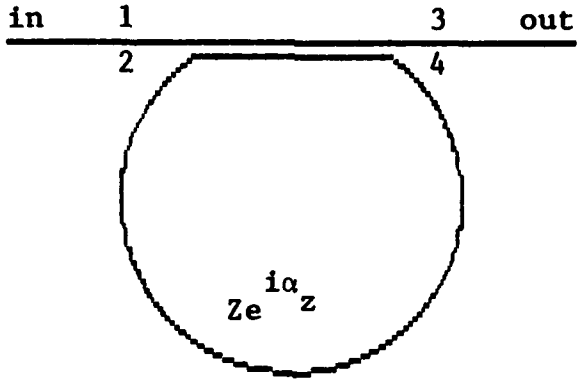

Figure 2: Two Fiber Supplemental Path Design

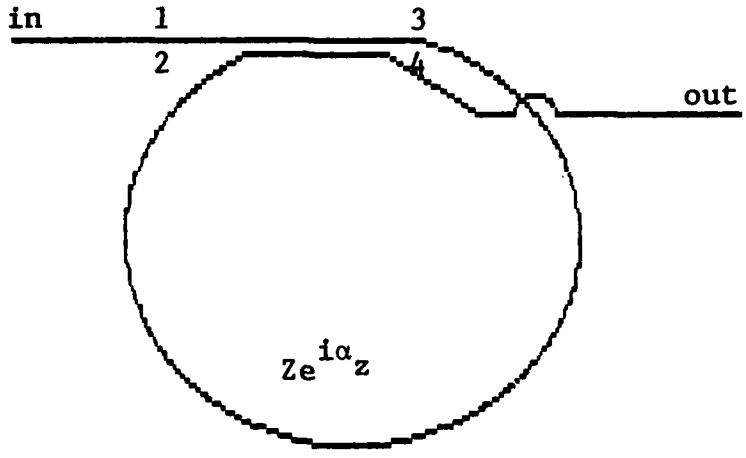

Figure 3: Single Fiber Supplemental Path Design

The method of Figure 3 is simply a way to introduce a phase shift without splicing or reflection loss. The transmission coefficient and phase for this method is described by the following equation:

$$\frac{E_4}{E_1} = \frac{ir + Ze^{i\alpha_z}}{1-irZe^{i\alpha_z}} \tag{21}$$

For the case of zero coupling, r=0, once again the output is completely determined by the loop characteristics:

$$\frac{E_4}{E_1} = Ze^{i\alpha_z} \tag{22}$$

V. DEVICE OUTPUT CHARACTERISTICS

The characteristics described in this section are based on the ideal case of zero coupler loss. Coupler loss effects will be discussed in the implementation section. We also assume that the device is under coherent excitation and the coherence length is longer than the resonant cavity length.

The transmittance of this device exhibits two fundamental output characteristics. There may be a dip in a relatively high output or a peak in a relatively low output. These both occur as a function of the coupling

values, transmission coefficients X_1 and X_2, and the loop phase P.

A. Dip in the Transmittance

This condition exists when the device is configured to give a high off-resonance transmittance, as shown in Figure 4. When the proper phase in the loop is achieved, the loop power builds up while the output power decreases. This dip is produced under two different device configurations yet their characteristics are very similar.

In the first case, the second coupler, CP2, acts to enhance the less than complete coupling of CP1. For this condition we set $X_1 = X_2 = 1$ and $\alpha_1 = \alpha_2 \approx 0$. Physically, this represents the removal of the supplemental paths. Examination of equations (9) and (16) show that resonance occurs for $P = 3\pi/2$, and under this condition the transmittance becomes:

$$T = \left| \frac{i(t_1 r_2 + r_1 t_2 - X_3)}{1 + iX_3(r_1 t_2 + r_2 t_1)} \right|^2 \qquad (23)$$

At this point it is interesting to relate equation (23) to the transmittance of a single coupler resonator. We can do this by letting $r_2 = 0$ and $t_2 = 1$ [9]:

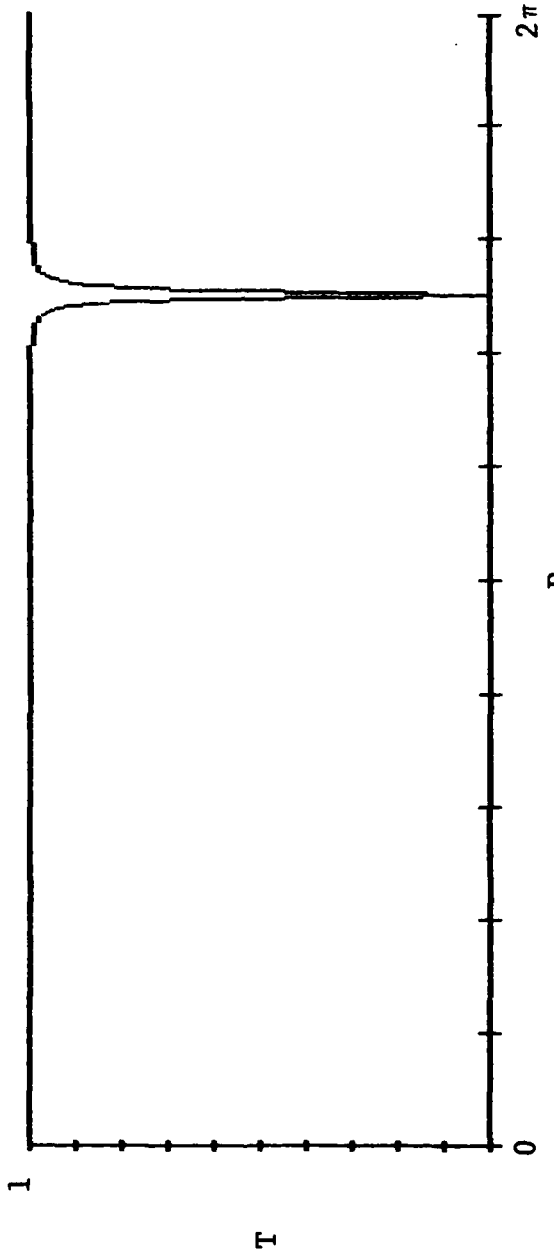

Figure 4: Dip in the Transmittance

$$T_s = \left| \frac{i(r_1 - X_3)}{1 + iX_3r_1} \right|^2 \qquad (24)$$

For this case the minimum occurs when $r_1 = X_3$. However, when the coupling value of r_1 is not comparable to X_3, the resonator finesse and dip magnitude are degraded. Fortunately, the addition of a second coupler, as illustrated in Figure 1, can be used to enhance the first coupler. Referring to equation (23), the new condition for transmittance minimum is:

$$t_1r_2 + r_1t_2 = X_3 \qquad (25)$$

Assuming zero coupler loss, we can use energy conservation to rewrite equation (25):

$$r_2\sqrt{1 - r_1^2} + r_1\sqrt{1 - r_2^2} - X_3 = 0 \qquad (26)$$

By inserting the known values of r_1 and X_3 we can find the required value for r_2. As an illustration, consider the following example:

NOTE: The loop power ratio is the ratio of power in the feedback loop to the input power.

Single Coupler Resonator:

$X_3 = .9999$

$r = .995$

$t = .0998749$

finesse = 617.245

transmittance minimum = .923287

loop power ratio maximum = 383.581

Enhanced Coupler Resonator:

r_2 = .086 (from equation 26)

t_2 = .996295

finesse = 21,000

transmittance minimum = .000217

loop power ratio maximum = 5,000

This increase in finesse causes the magnitude of the transmittance minimum to become more sensitive to the loss in the loop. Figures 5 and 6 are plots of the transmittance minimum versus X_3 for the single and enhanced resonator configurations respectively.

The second case of dip in the output occurs when the coupling at CP1 equals the coupling at CP2 such that:

$$r_1 t_2 = r_2 t_1 = A \tag{27}$$

The associated device parameters are as follows: $X_1 = X_2 = 1$ and $\alpha_1 = \alpha_2$. At resonance the transmittance is given by equation (23). However, in this case we note that the transmittance minimum occurs for:

$$A = X_3/2 \tag{28}$$

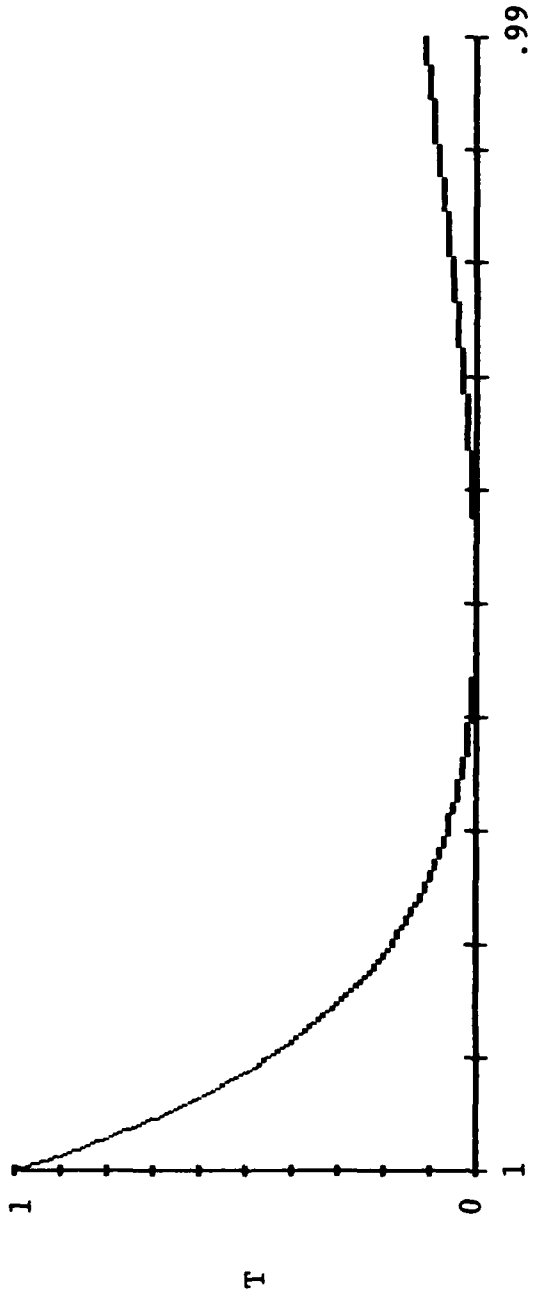

Figure 5: Transmittance at Resonance vs. X_3 for the Single Coupler Resonator

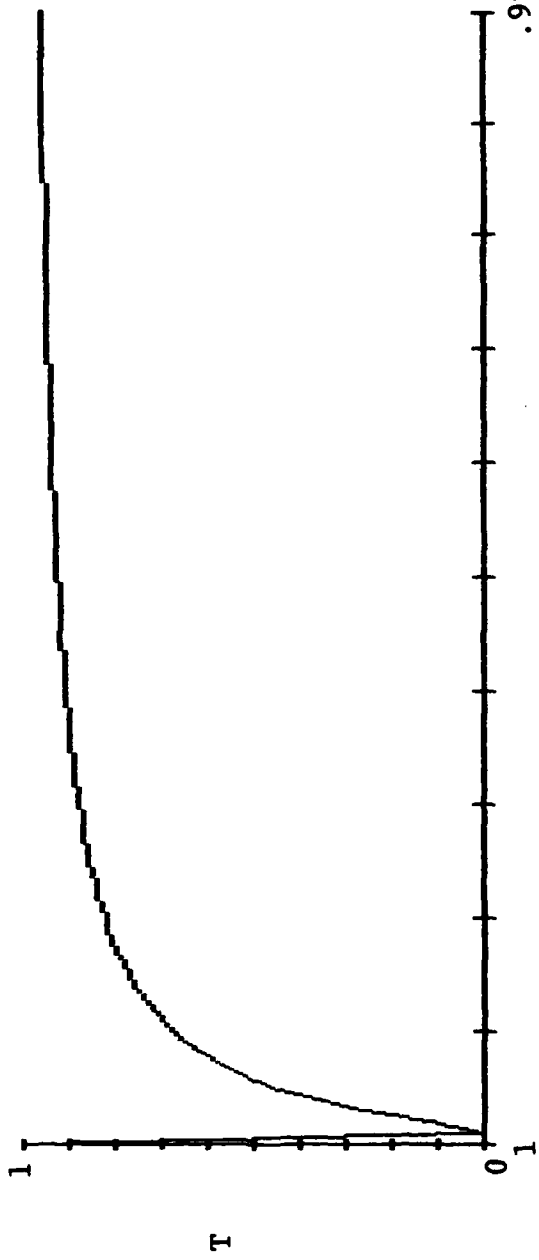

Figure 6: Transmittance at Resonance vs. X_3 for the Enhanced Coupler Resonator

Knowing that the coupling values are equal and applying conservation of energy we can derive the following relationship between r and X_3:

$$r^4 - r^2 + \frac{X_3}{4} = 0 \qquad (29)$$

Equation (29) shows that for any fiber loss we can find an appropriate coupling value which will minimize the resonant transmittance. An X_3 of .9999 yields a coupling value of r = .712 while X_3 = .99 yields r = .7553. Figures 7 and 8 show the plots of transmittance minimum versus X_3 for r = .712 and r = .7553 respectively. Unfortunately, the finesse is still dominated by the loop transmission X_3. Therefore, even though we can optimize r, the finesse continues to degrade as X_3 decreases. This is illustrated by the following example:

X_3 = .9999

r = .712

t = .7022

finesse = 21,000

transmittance minimum = .000328

loop power ratio maximum = 4,998

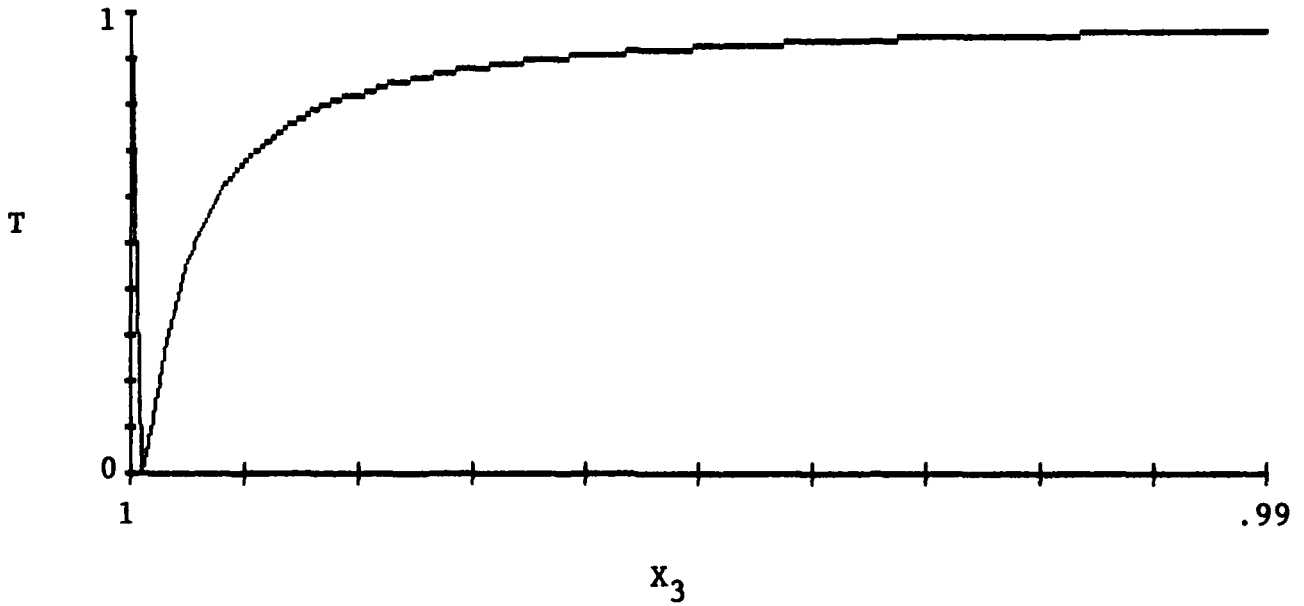

Figure 7: Transmittance at Resonance vs. X_3 for the Equivalent Coupler Resonator, r = .712.

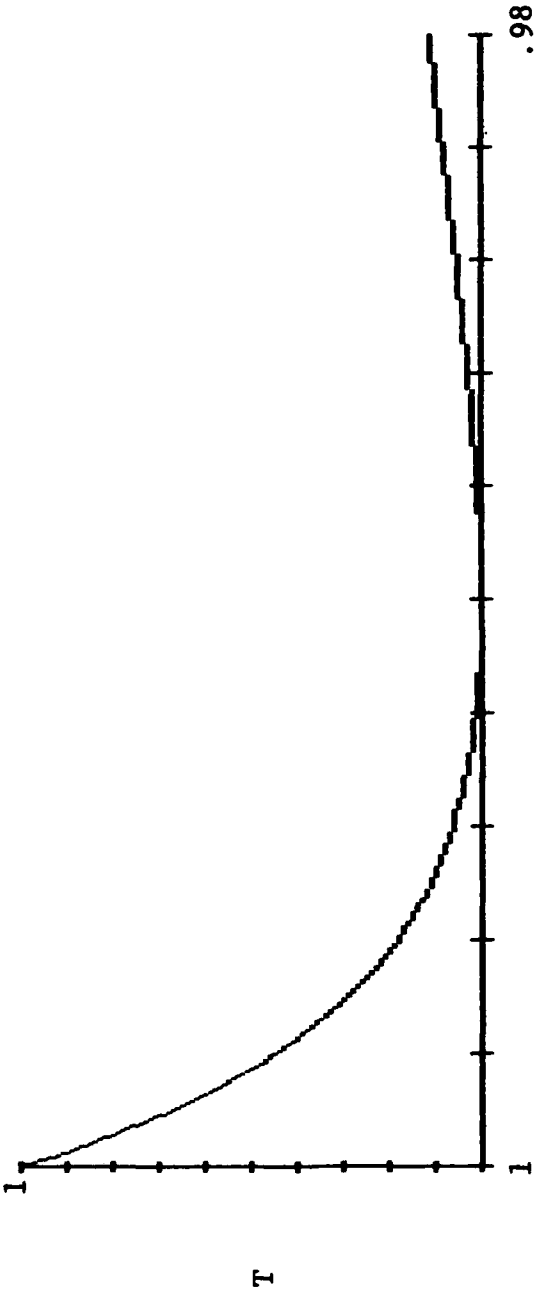

Figure 8: Transmittance at Resonance vs. X_3 for
The Equivalent Coupler Resonator, r = .7553

$X_3 = .99$

$r = .7553$

$t = .65538$

finesse = 165

transmittance minimum = 6.343×10^{-7}

loop power ratio maximum = 50.25

Up to this point we have assumed that $\alpha_1 = \alpha_2$; however, the transmittance varies when this is not true. For $\alpha_1 \neq \alpha_2$ the location of the transmittance minimum changes with respect to P as a function of $|\alpha_1 - \alpha_2|$. In addition, as the location of the minimum changes, the magnitude of the transmittance minimum as well as the finesse decreases. This is illustrated in Figure 9 where α_1 is held constant and α_2 varies as shown.

B. Peak in the Transmittance

This unique condition exists when the device is configured to give a low off-resonance transmittance. Figure 10 shows a plot of this output. The device parameters which cause this output are listed below:

-- "strong" coupling at CP1, $r_1 > .9$

-- "weak" coupling at CP2, $r_2 < .1$

-- $X_1 = 1$, $X_2 = 0$

-- α_1 arbitrary

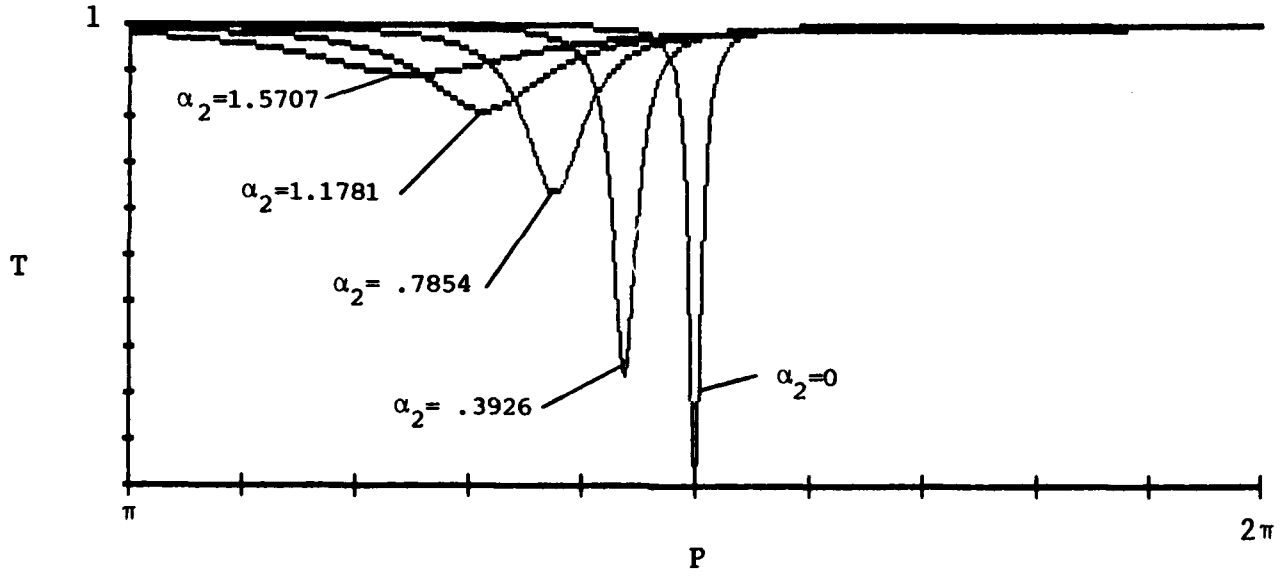

Figure 9: Transmittance for Variation in $|\alpha_1 - \alpha_2|$ α_1 = 0 and α_2 is as indicated. Values are in radians.

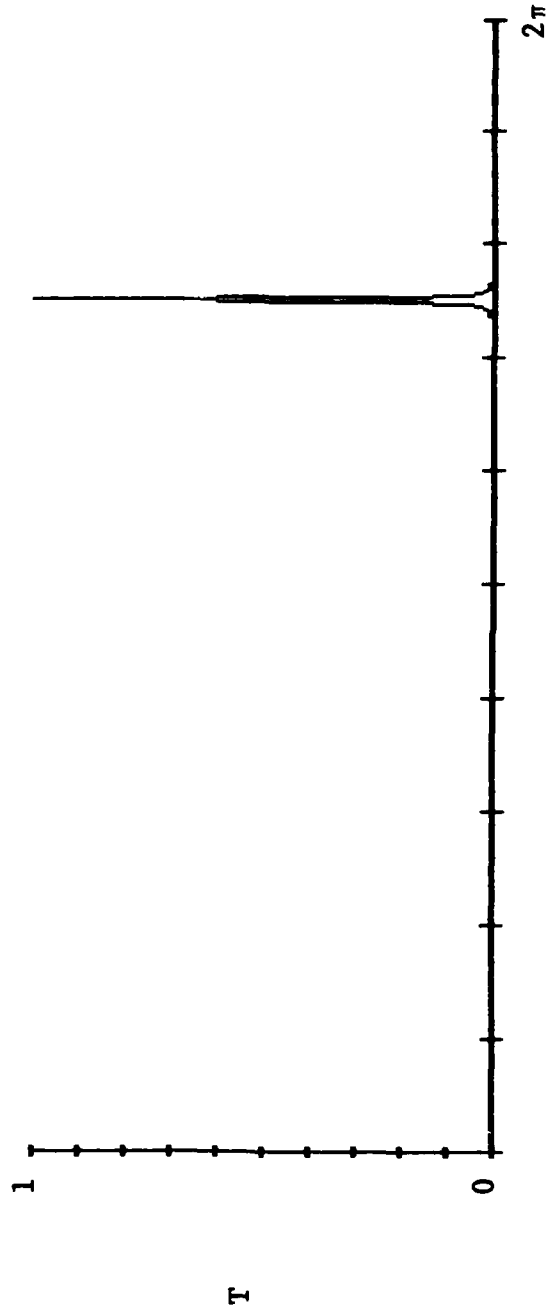

Figure 10: Peak in the Transmittance

For the parameters listed above and at resonance, the transmittance is given by:

$$T = \left| \frac{r_2 t_1}{1 - X_3 r_1 t_2} \right|^2 \qquad (30)$$

Solving this equation for maximum transmittance, T = 1, and applying conservation of energy yields the following relationship:

$$r_2\sqrt{1 - r_1^2} + X_3 r_1\sqrt{1 - r_2^2} - 1 = 0 \qquad (31)$$

Unfortunately, this equation only has real solutions when $X_3 = 1$. The effect of X_3 on equation (31) is illustrated by the following calculations:

$X_3 = 1$, $r_1 = .995$

From equation (31), $r_2 = .099878$

$$r_2\sqrt{1 - r_1^2} + X_3 r_1\sqrt{1 - r_2^2} - 1 = 0$$

$X_3 = .9999$, $r_1 = .995$

$r_2 = .099878$

$$r_2\sqrt{1 - r_1^2} + X_3 r_1\sqrt{1 - r_2^2} - 1 = -1 \times 10^{-4}$$

The previous calculations confirm that although we can minimize equation (31) for $X_3 \neq 1$, real solutions do not exist unless $X_3 = 1$.

Finally, variation of the phase α_1 just changes the location of the peak with respect to P. The magnitude and finesse are unaffected by this variation.

VI. EFFECTS OF MODULATING P

Modulation of the phase shift P in the feedback loop represents a simple method of exploiting the characteristics described in Section V. Simple sinusoidal modulation, for example, with a PZT crystal results in a multiple dip/peak output in the transmittance wave form. The general form of this modulation is:

$$P = A\sin(wt + \phi) + B \qquad (32)$$

The amplitude coefficient A determines the number of dips/peaks in the output waveform. It also has a small effect on the dip/peak width due to its effect on the slope of the sinusoid. ϕ is a phase bias which determines the zero crossing point of the sinusoid. This affects the dip/peak width and the distance between dips/peaks. The phase bias B, which is external to the sinusoid, effectively centers the modulation about some

desired point. Changes in B have approximately the same effect as changes in ϕ.

It is apparent that even this simple modulation scheme can have complicated effects on the transmittance waveform. For our calculations we will let w = 1, f = 1/2 πHz, and therefore our time scale will be in seconds. In the applications section, the applied modulation will be:

$$P = 3.5 \cos(t) - \pi/2 \qquad (33)$$

This form is convenient in that it is centered at the resonance point and produces a transmittance waveform with a period equal to π seconds. In addition, the dip/peak resolution is identical to that produced under a ramp phase modulation.

The Fourier analysis in the applications section is based on this modulation scheme. A method for determining the spectrum for general modulation is given in the Appendix.

VII. IMPLEMENTATION CONSIDERATIONS

This section contains information necessary for the realistic computer simulation of this device and its actual implementation. In previous sections two

primary sources of loss had been ignored, coupler loss and fiber attenuation. Data gathered from the literature will be used to incorporate these losses into our calculations. The resulting information will then be representative of the current state of the art and model a realistic device.

Recent advances in optical fiber fabrication technology has resulted in a new generation of low loss fiber [4, 5]. To avoid placing too severe a restriction on the device design, we chose a fairly common fiber loss value of .2 db/km [13]. Choosing a fiber loop length of one meter makes the loop transmission X_3 equal .99997697. Therefore in our calculations we will use the value:

$$X_3 = .9999 \tag{34}$$

Coupler loss as it applied to a one coupler resonator was discussed in Section II. Since our device consists of two couplers with different coupling values, we will refer to reference [7] for the coupler loss values. Given the desired r, the corresponding γ can be inserted into equation (1) to determine the required t value. These numbers will then be used in the transmittance calculations.

When coupler loss values are included in the energy conservation equation, then real solutions do not exist for equations (26), (29), and (31). However, optimum values can be found and these will be used in our calculations. From this point on the various resonator configurations, optimized with losses included, will be referred to by the following designations:

Configuration A (Single Coupler, Transmittance Dip)

$r = .995$

$t = .09206$

$\gamma = .15\%$

Configuration B (Transmittance Dip)

$r_1 = .995$ $\quad r_2 = .09$

$t_1 = .09206$ $\quad t_2 = .99368$

$\gamma_1 = .15\%$ $\quad \gamma_2 = .45\%$

Configuration C (Transmittance Dip)

$r_1 = r_2 = .712$

$t_1 = t_2 = .7$

$\gamma_1 = \gamma_2 = .3\%$

Configuration D (Transmittance Peak)

$r_1 = .998$ $\quad r_2 = .0632$

$t_1 = .04996$ $\quad t_2 = .99549$

$\gamma_1 = .15\%$ $\quad \gamma_2 = .5\%$

In Section V we examined the characteristics for configurations A, B, and C without losses. The characteristics with losses included are listed below:

	A	B	C
finesse	617.00	1023.0	976.00
transmittance minimum	0.9733	0.8754	0.8806
loop power ratio maximum	325.00	0.3861	27.000

It is interesting to note that configurations B and C are greatly affected by the addition of coupler loss. This is because the lower coupling values required have a correspondingly higher coupler loss. Nevertheless, they represent a significant improvement over the single coupler design. Plots of the transmittance minimum versus X_3 for configurations A, B, and C are shown in Figures 11, 12, and 13 respectively.

The most surprising result of these calculations was the decline in loop power ratio maximum for configurations B and C. Although the finesse is approximately 166 percent of configuration A, the loop power ratio is less than 1 percent of configuration A.

Configuration D was discussed in Section V and it was determined that even with zero coupler loss, real solutions for r_2 exist only when $X_3 = 1$. Therefore,

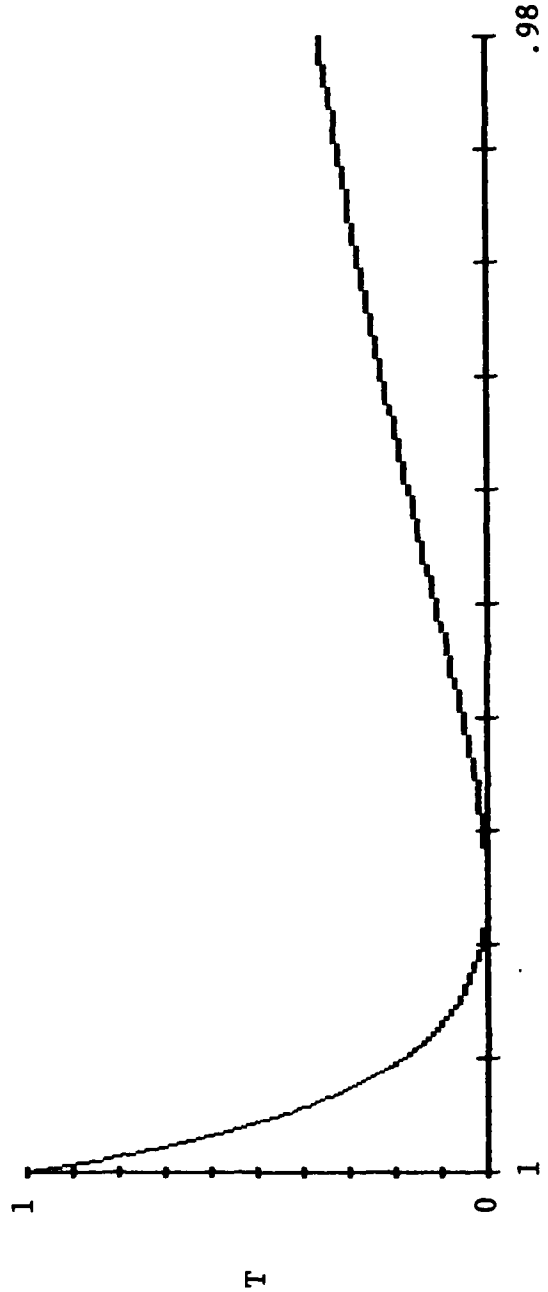

Figure 11: Transmittance at Resonance vs X_3 for Configuration A.

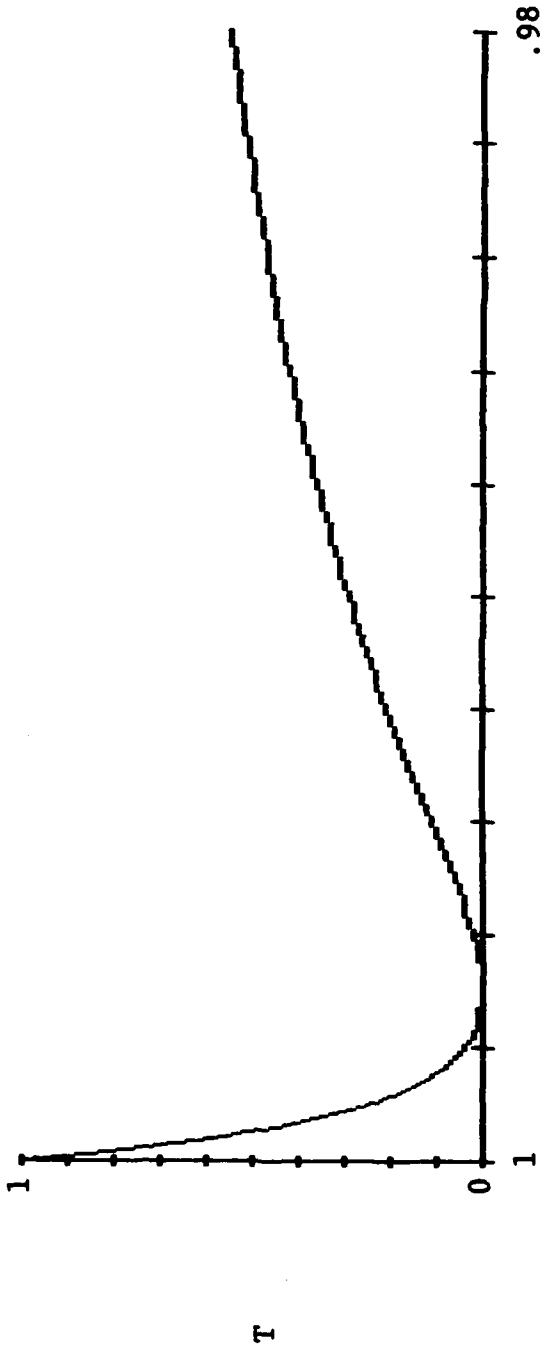

Figure 12: Transmittance at Resonance vs X_3 for Configuration B.

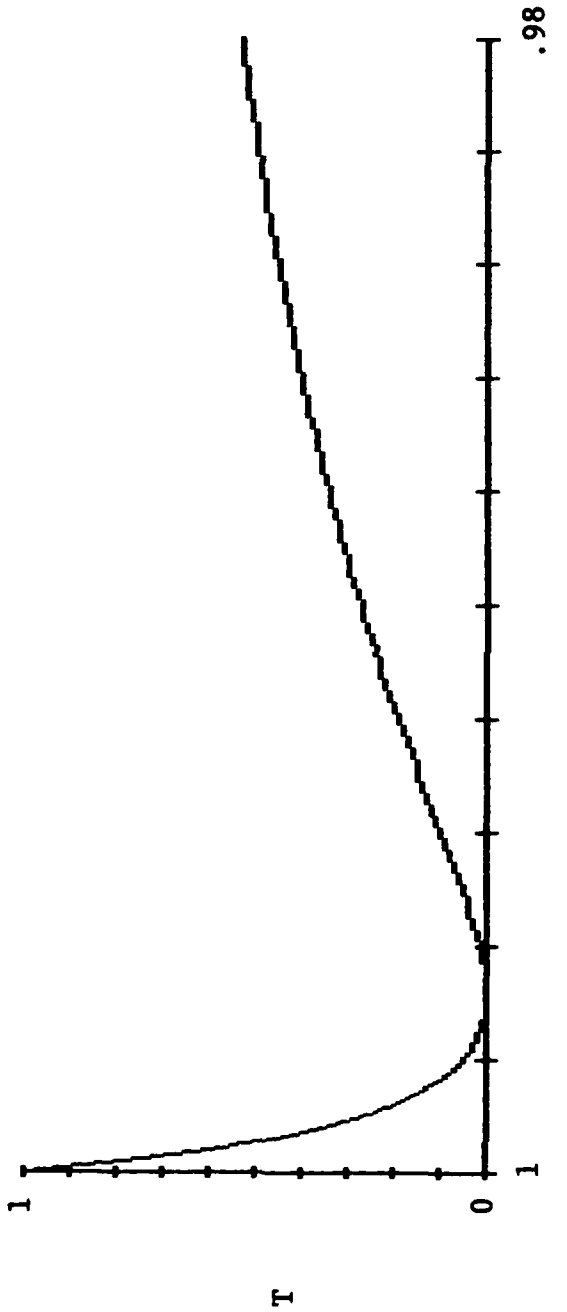

Figure 13: Transmittance at Resonance vs X_3 for Configuration C.

we assumed a one centimeter loop length which yields X_3 = .9999995. Comparison of the idealized calculations to the realistic ones are shown below:

Ideal Case ($X_3 = 1$)

$r_1 = .998$ $\quad$ $r_2 = .0632$

$t_1 = .0632$ $\quad$ $t_2 = .998$

$\gamma_1 = 0$ $\quad$ $\gamma_2 = 0$

finesse = 791

transmittance maximum = 1.0

loop power ratio maximum = 250

Realistic Case ($X_3 = .9999995$)

Configuration D

finesse = 482

transmittance maximum = .236

loop power ratio maximum = 59

Therefore, it does not appear that this configuration has any immediately useful characteristics.

VIII. APPLICATIONS

It is obvious that this device has a number of potential applications. In this section we will examine the use of configurations B and C as microbend

sensors. Potential application as a laser gyroscope will also be introduced.

Microbend sensors are based on producing a change in transmission along an optical path. This change in transmission is proportional to some applied force and is due to the microbends induced in the fiber by that force. In reference [16], an analysis of the change in transmittance of a fiber due to a single microbend is reported. The study reports an approximately quadratic relationship between insertion loss in dB and microbend amplitude in micrometers. Applying a quadratic best fit to the tabular data we can approximate the insertion loss for small distortion amplitudes. This relationship is given by:

$$IL = (2.5333 \times 10^{-4})\ DA^2 + (6.6667 \times 10^{-5})\ DA \quad (35)$$

where: IL = insertion loss in dB
DA = distortion amplitude in um

If we assume that this insertion loss takes place in our feedback loop, then we can relate IL to X_3 by the following equation:

$$IL = -10 \log \left| \frac{X_3^2}{.9998} \right| \quad (36)$$

Finally, we can use equations (36) and (35) to write a quadratic equation in terms of X_3 and DA only:

$$DA^2 + (263.1596 \times 10^{-3})\ DA + \frac{10 \log\left|\frac{X_3^2}{.9998}\right|}{(2.5333 \times 10^{-4})} = 0 \quad (37)$$

Using equation (37), we can determine the relationship between the distortion amplitude of a single microbend in our feedback loop and the change in output transmittance. Referring to Figures 5 and 6, we see that both configurations B and C are approximately linear over the range X_3 = .9999 to X_3 = .999. Tables 1 and 2 show the variation in transmittance versus the loop transmission X_3 for both configurations. Using equation (37), this range compares to a distortion amplitude range of 0 to 9.85 micrometers. If we assume a relatively low input power of 1mW, then the output power ranges are listed below:

Configuration B: .875416 mW to .250749 mW

Configuration C: .880633 mW to .267967 mW

The sensitivity of this device is limited theoretically by the quantum noise limit and realistically by the system noise. Since the system noise is

TABLE 1. CONFIGURATION B

LOOP X3	TRANSMITTANCE	LOOP X3	TRANSMITTANCE
0.999900	0.875415917980	0.999450	0.477098139705
0.999882	0.854678049932	0.999414	0.465406410787
0.999864	0.834421670525	0.999414	0.453974534365
0.999828	0.795304326216	0.999378	0.431866486022
0.999810	0.776419753966	0.999360	0.421178784610
0.999792	0.757969430036	0.999342	0.410727866912
0.999774	0.739942412349	0.999324	0.400508343438
0.999756	0.722328082158	0.999306	0.390514966571
0.999738	0.705116132933	0.999288	0.380742626246
0.999720	0.688296559685	0.999270	0.371186345779
0.999702	0.671859648710	0.999252	0.361841277835
0.999684	0.655795967728	0.999234	0.352702700547
0.999666	0.640096356409	0.999216	0.343766013752
0.999648	0.624751917261	0.999198	0.335026735368
0.999648	0.624751917261	0.999198	0.335026735368
0.999630	0.609754006868	0.999180	0.326480497894
0.999612	0.595094227462	0.999162	0.318123045017
0.999594	0.580764418814	0.999144	0.309950228349
0.999576	0.566756650432	0.999126	0.301958004261
0.999558	0.553063214055	0.999108	0.294142430830
0.999540	0.539676616423	0.999090	0.286499664887
0.999522	0.526589572314	0.999072	0.279025959156
0.999504	0.513794997849	0.999054	0.271717659498
0.999486	0.501286004032	0.999036	0.264571202237
0.999468	0.489055890535	0.999018	0.257583111578
0.999450	0.477098139705	0.999000	0.250749997107

TABLE 2. CONFIGURATION C

LOOP X3	TRANSMITTANCE	LOOP X3	TRANSMITTANCE
0.999900	0.880632937486	0.999450	0.493466010325
0.999882	0.960694080204	0.999432	0.481942031258
0.999864	0.841198048476	0.999414	0.470663204232
0.999846	0.822133964038	0.999396	0.459624086000
0.999828	0.803491262739	0.999378	0.448819373570
0.999810	0.785259683985	0.999360	0.438243900023
0.999792	0.767429260581	0.999342	0.427892630459
0.999774	0.749990308971	0.999324	0.417760658096
0.999756	0.732933419839	0.999306	0.407843200491
0.999738	0.716249449080	0.999288	0.398135595891
0.999720	0.699929509099	0.999270	0.388633299708
0.999702	0.683964960446	0.999252	0.379331881108
0.999684	0.668347403754	0.999234	0.370227019718
0.999666	0.653068671988	0.999216	0.361314502439
0.999648	0.638120822970	0.999198	0.352590220365
0.999630	0.623496132188	0.999180	0.344050165800
0.999612	0.609187085858	0.999162	0.335690429379
0.999594	0.595186374251	0.999144	0.327507197277
0.999576	0.581486885252	0.999126	0.319496748510
0.999558	0.568081698158	0.999108	0.311655452322
0.999540	0.554964077691	0.999090	0.303979765661
0.999522	0.542127468239	0.999072	0.296466230728
0.999504	0.529565488282	0.999054	0.289111472610
0.999486	0.517271925038	0.999036	0.281912196985
0.999468	0.505240729275	0.999018	0.274865187902
0.999450	0.493466010325	0.999000	0.267967305627

almost impossible to predict, we will use the literature to determine a baseline value. In reference [21] a minimum detectable optical power of 3.4×10^{-12}W was reported. Using this as a guideline, we can approximate the sensitivity of our devices. Tables 3 and 4 list the variation in transmittance, for configurations B and C respectively, over the range $X_3 = .9999$ to $X_3 = .99989999$ in increments of 1×10^{-9}. Using equation (37) we find that one increment corresponds to a distortion amplitude of .13 nanometers. Assuming the same input power of 1mW, the corresponding change in output power is:

Configuration B: P = 1.16 nW per .13 nanometers

Configuration C: P = 1.12 nW per .13 nanometers

These values are well within current detectability ranges even with moderate noise in the system.

We will not attempt to relate the distortion amplitude to the required applied force since that is a function of the transducer design. However, we will point out that these values are for a single microbend and therefore a phenomenal increase in sensitivity can be expected when a typical microbend grating is used [2, 3].

TABLE 3. CONFIGURATION B

LOOP X3	TRANSMITTANCE	LOOP X3	TRANSMITTANCE
0.999000000	0.875675625265	0.999899995	0.875669832188
0.999899999	0.875674325733	0.999899994	0.875668532665
0.999899998	0.875673202341	0.999899993	0.875667409287
0.999899997	0.875672078955	0.999899992	0.875666285907
0.999899996	0.875670955573	0.999899991	0.875665162536
0.999899995	0.875669832188	0.999899990	0.875663863018

TABLE 4. CONFIGURATION C

LOOP X3	TRANSMITTANCE	LOOP X3	TRANSMITTANCE
0.999900000	0.880726767376	0.999899995	0.880721193499
0.999899999	0.880725685028	0.999899994	0.880720111157
0.999899998	0.880724440529	0.999899993	0.880718866669
0.999899997	0.880723358182	0.999899992	0.880717784327
0.999899996	0.880722275838	0.999899991	0.880716701995
0.999899995	0.880721193499	0.999899990	0.880715619661

As an example of how our system can increase the sensitivity of current microbend detection sensor systems we examine the data in reference [17]. This article reports the design of a wide-range strain sensor which uses a roller chain to impose microbends rather than the typical corrugated plate. The roller chain was used to increase the detection range, however it also reduced sensitivity. The authors reported a linear relationship between sensor displacement and light transmission. This relationship is given by the following equation:

$$D = \frac{\Delta T}{1.25} \tag{38}$$

where: D = linear displacement in inches
ΔT = change in light transmission.

If this transducer were placed in our one meter feedback loop, then equation (38) would become:

$$D = \frac{(.9999 - X_3)}{1.25} \tag{39}$$

Recalling that our linear range is approximately X_3 = .9999 to X_3 = .999, equation (39) gives a displacement range of 0 to 18.3 micrometers. If we assume the same input power, 1mW, then the output power range is the same

as the previous application. The sensitivity can be approximated by referring to Tables 3 and 4, and plugging the increment value, $X_3 = 1 \times 10^{-9}$, into equation (39). This gives a displacement sensitivity of approximately 20.32 picometers. Therefore, by placing this low sensitivity transducer in our feedback loop, we now have an ultrasensitive linear displacement detector.

Because of fluctuations in the input power level, the use of intensity as the measurement parameter requires an additional isolated reference path for comparison. Should noise levels in the system become substantial enough to affect the required sensitivity, it may be necessary to use the spectrum of the transmittance output for detection. The magnitudes of the first 10 harmonics for configurations B and C are shown in Figures 14 and 15 respectively. The loop modulation is $P = 3.5 \cos(t) - \pi/2$. When we isolate a single harmonic for power measurement we eliminate a majority of the noise. If we assume a 1 mW power input then the power in the first harmonic versus X_3 is as shown below:

X_3	Configuration B	Configuration C
.9999	.01822117 mW	.01821135 mW
.9998	.01845245 mW	.01843529 mW

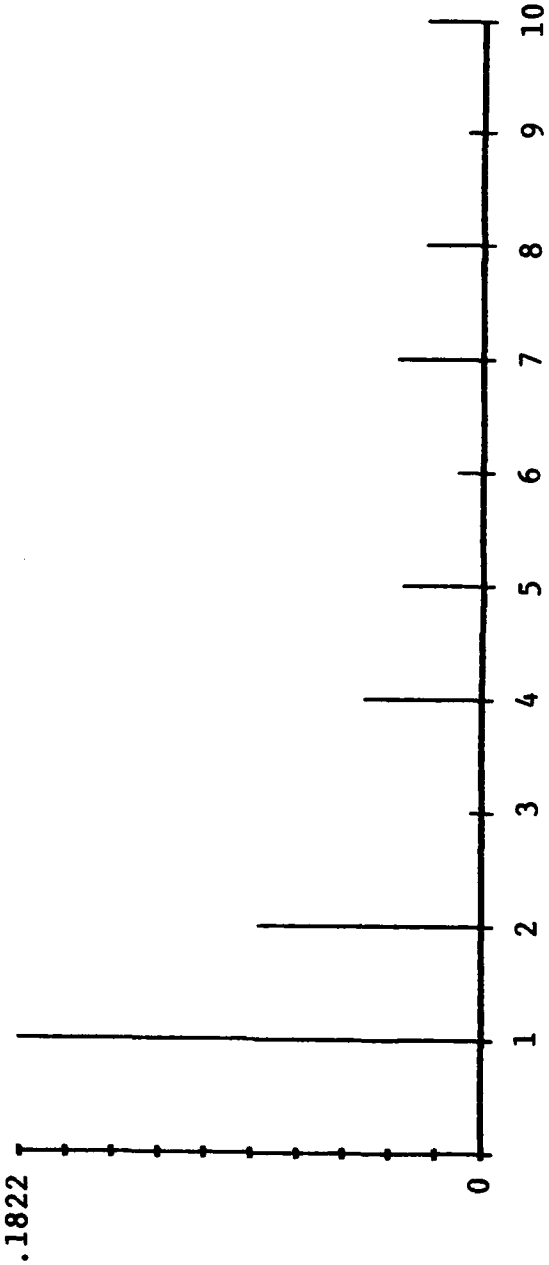

Figure 14: Magnitudes of the First 10 Harmonics for Configuration B.

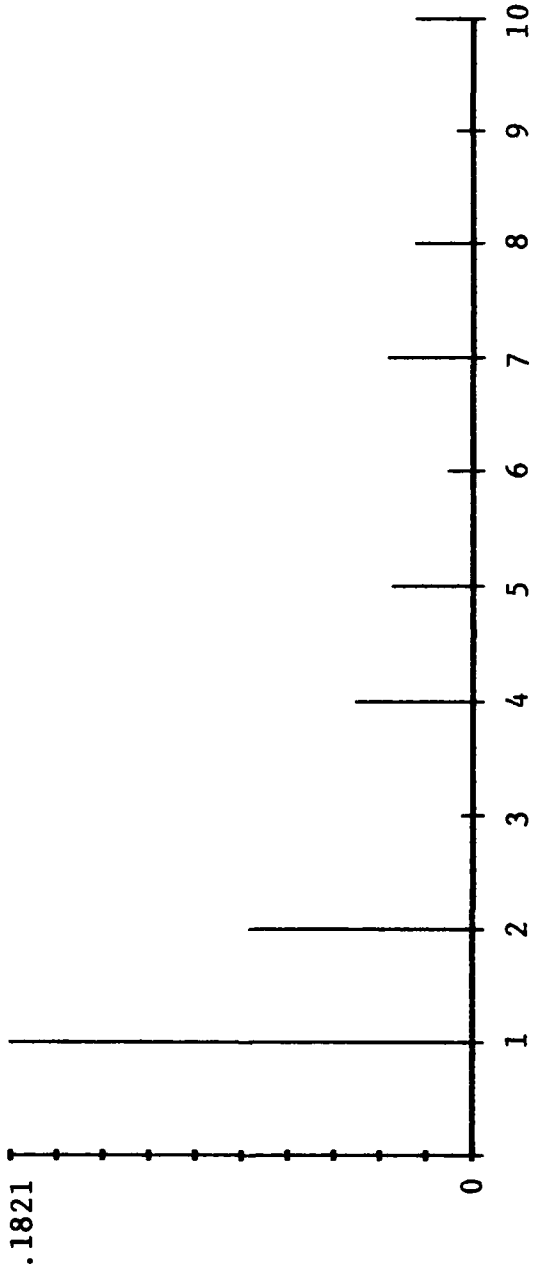

Figure 15: Magnitudes of the First 10 Harmonics for Configuration C.

As a comparison, the required power sensitivity for intensity detection and harmonic detection for configurations A, B, and C are shown below:

($\Delta X_3 = 1 \times 10^{-8}$, input power = 1 mW)

	Intensity	Harmonic
Configuration A	P = 7.37 nW	P = 17.7 pW
Configuration B	P = 11.66 nW	P = 25.9 pW
Configuration C	P = 11.20 nW	P = 25.9 pW

Although the spectrum detection method requires more sensitivity, it may be able to offset the effects of a noisy system.

Another possible application of this device is as a laser gyroscope. If we assume an axis of rotation normal to the feedback loop, then to the first order the Sagnac phase shift is given by:

$$\phi_s = \frac{4\pi NA}{\lambda C}\Omega \qquad (40)$$

where: ϕ_s = Sagnac phase shift

A = the area of one turn in the coil

N = number of turns in the coil

λ = free space wavelength

C = speed of light in free space

Ω = angular velocity

Equation (40) shows that the magnitude of the induced phase shift is directly proportional to the length of the loop. Using the same fiber as previously, we let the length of the loop be 130.5 meters which corresponds to an X_3 of .997. If we examine the transmittance waveform with $P = 3.5 \cos(t) - \pi/2$ over the range of $t = 0$ to $t = 2\pi$, we notice there are two dips; one is located at $t = \pi/2$ and the other at $t\ 3\pi/2$. This is illustrated in Figure 16. Letting the loop rotate about its normal axis causes the modulation to become:

$$P = 3.5 \cos(t) - \pi/2 + \phi_s \qquad (41)$$

The useful characteristic of configurations B and C is that the time between dips varies as a function of ϕ_s. Listed below are the changes in time between dips versus small ϕ_s:

ϕ_s(rad)	Configuration B	Configuration C
.001	$\Delta t = 5.717 \times 10^{-4}$	$\Delta t = 5.717 \times 10^{-4}$
.0001	$\Delta t = 5.65 \times 10^{-5}$	$\Delta t = 5.579 \times 10^{-5}$
.00001	$\Delta t = 7.39 \times 10^{-6}$	$\Delta t = 6.91 \times 10^{-6}$

If we use a source with $\lambda = 1$ micrometer and a total loop length of 130.5 meters, then we can use equation (40) to calculate the corresponding rotation rates. If we assume

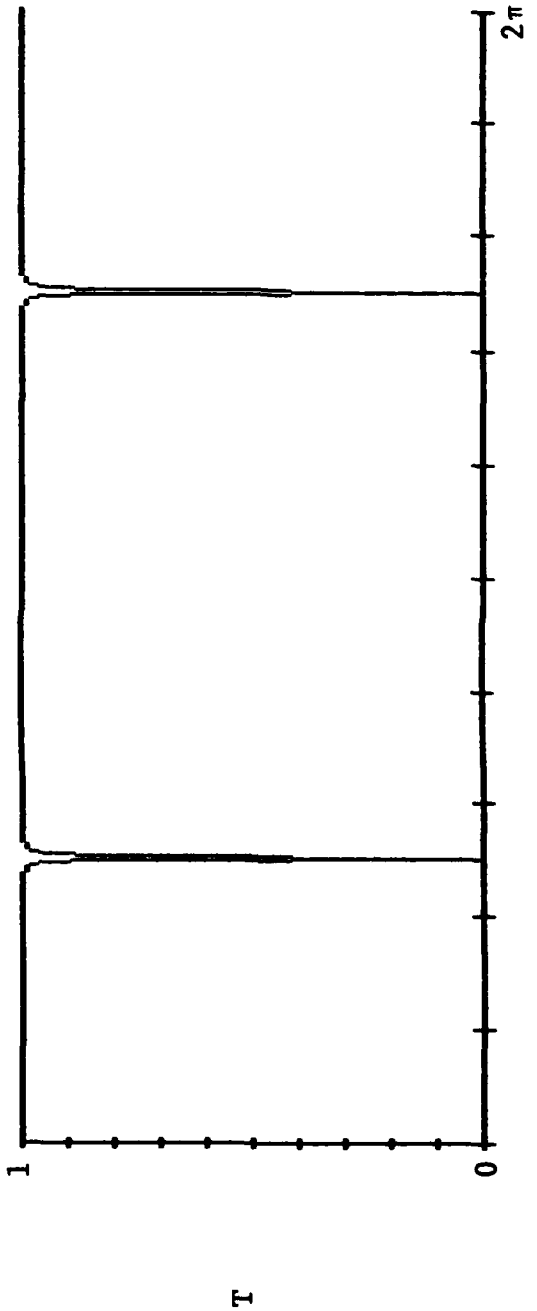

Figure 16: Transmittance vs P for the Modulation
P = 3.5cos(t) - π/2

a modulation frequency of 1 KHz, then we have the following relationships between rotation rate and time change between dips:

Ω (10^{-6} $\frac{rad}{s}$)	Configuration B	Configuration C
17.600	Δt = 571.70 ns	Δt = 571.70 ns
1.760	Δt = 56.50 ns	Δt = 55.79 ns
.176	Δt = 7.39 ns	Δt = 6.91 ns

Since inertial rotation sensing requires sensitivities on the order of 1 microradian per second, our device is an ideal candidate for this type of application. The major benefit being the use of a single propagating beam which makes this device immune to the nonreciprocal effects that plague counterpropagating beam rotation sensors. Additionally, the low loop power at resonance will help to minimize the nonlinear noise in the system and improve stability.

IX. OPTICAL PHASE CHARACTERISTICS

Up to this point we have dealt only with the magnitude characteristics of the transmittance. In this section we briefly describe the optical phase characteristics that may bear further investigation.

At resonance, this device undergoes a 2π phase shift. This is illustrated in figures 17 and 18 for configurations B and C respectively. It appears that each configuration has a different yet unique response to the phases in the supplemental paths α_1 and α_2.

Configuration B has an optical phase shift which is directly proportional to the phase difference $|\alpha_1 - \alpha_2|$. This phase shift is given by the following simple equation:

$$\Phi = \pi/2 + |\alpha_1 - \alpha_2| \qquad (42)$$

If the supplemental paths are wound in opposite directions then the Sagnac induced phase shift in one path would be $+\phi_s$ while the oppositely wound path would undergo a phase shift of $-\phi_s$. Referring to equation (42) we see that this configuration could operate as a laser gyroscope where the net optical phase shift is given by:

$$\Phi = \pi/2 + 2\,\phi_s \qquad (43)$$

where: ϕ_s = Sagnac induced phase shift.

Since the optical output phase is directly proportional to the rotation induced phase shift, the sensitivity is limited only by our ability to detect small changes in optical phase.

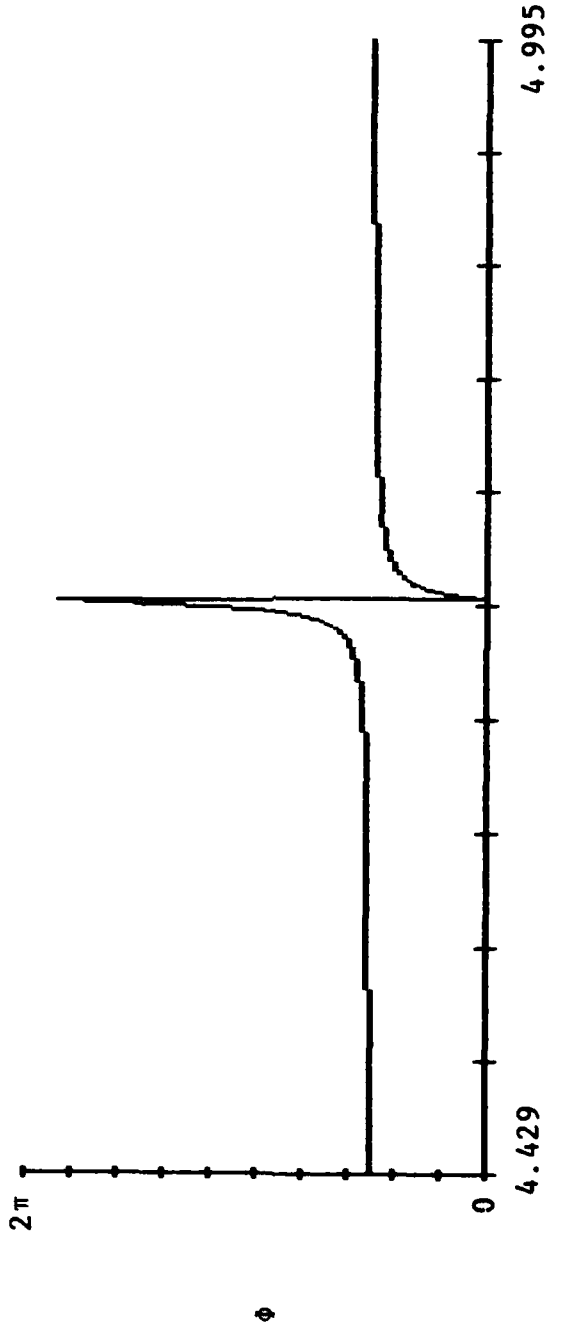

Figure 17: Optical Phase Shift vs P for Configuration B

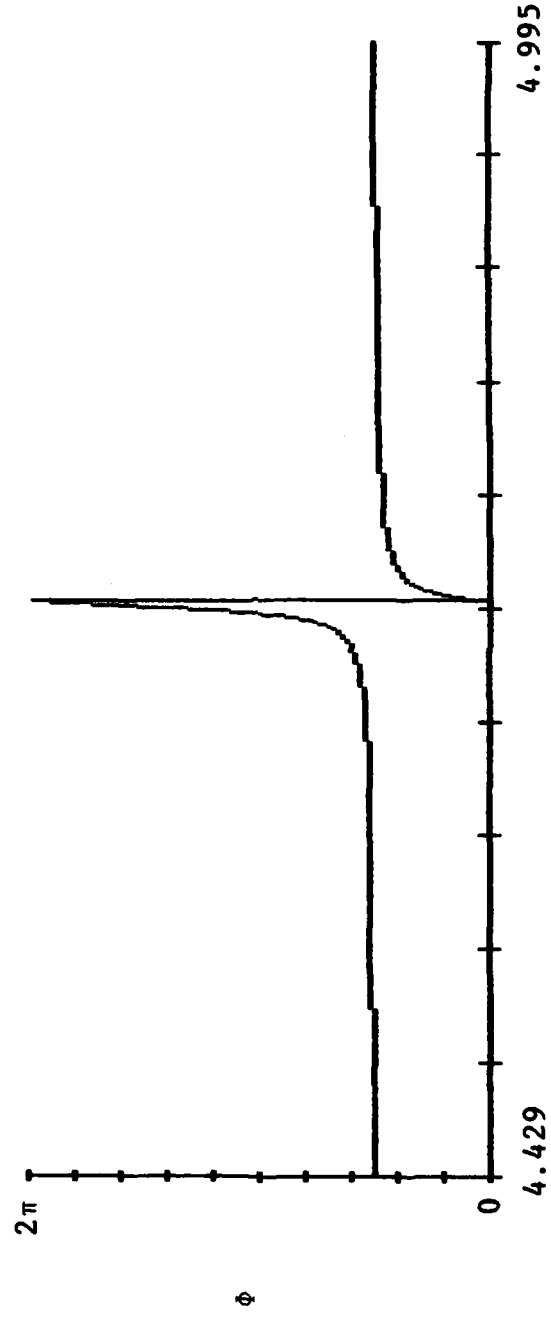

Figure 18: Optical Phase Shift vs P for Configuration C.

Configuration C also has an optical phase shift which is proportional to the phase difference $|\alpha_1 - \alpha_2|$. Unfortunately, there does not appear to be the same direct relationship shown in equation (43). There is however an additional relationship between the rate of change of the optical phase shift at resonance and the phase difference $|\alpha_1 - \alpha_2|$. Although the exact relationship is unknown, there appears to be a linear correspondence.

X. CONCLUSION

The two coupler resonator described in this thesis has a number of unique characteristics. It presents new ways to implement old concepts and introduces new phenomena with many potential applications.

State of the art single coupler resonators are constrained by the amount of light that can be coupled into the resonant loop. Our device presents two ways to overcome that restriction by introducing effective coupling values. These are listed below for configurations B and C respectively:

$$r_{eff} = r_1 t_2 + r_2 t_1 \tag{44}$$

$$r_{eff} = 2rt \tag{45}$$

Both configurations outperform the single coupler resonator yet appear to be equally simple to fabricate. Should a coupling technique be discovered that allows low coupling values and low loss then the performance of both configurations B and C will be phenomenal.

As is true of all resonators, this device is extremely sensitive to losses in the loop. That makes it particularly useful as a microbend sensor. In section VIII we showed a typical S/N limited sensitivity to a single microbend of amplitude .13 nanometers and in a separate case showed a sensitivity to a linear displacement of 20.32 picometers. Although these values were interpolated from the literature, they do indicate the potential capability of this device.

There are at least two ways this device can be used to detect rotation. Both are immune to the nonreciprocal effects suffered by rotation sensors using counter-propagating beams because they have low loop power maximums. This reduces the noise effects due to Rayleigh scattering and optical Kerr effect. In section VIII we discussed a way to detect rotation by measuring the time between dips. A rotation rate of .17 microradians per second corresponded to a time change of 7

nanoseconds. This is ideal for inertial rotation sensing. In section IX we stated that the optical phase shift in configuration B can be made directly proportional to twice the Sagnac phase shift. The sensitivity of this method is limited only by optical phase detection capability.

Although this thesis is theoretical in nature, much of the modeling is representative of experimental results reported in the literature. Therefore, upon fabrication, we should not expect to find a great deal of deviation from the values reported here. Because of the simplicity of the device, particularly configurations B and C, construction should be a straight forward process.

APPENDIX

In general, the modulation of P in the feedback loop will produce multiple dips/peaks in the output. Only in the special case used in this thesis are there just two dips/peaks a distance π apart. For the case of random distribution the period is 2π and the following method can be used to calculate the spectrum.

1. Calculate the spectrum of a single dip/peak as if it were alone in the period.
2. Determine the time between the initial peak and every other peak within the period.
3. The total spectrum is calculated by the following equation:

$$G_t = g(w)\{1 + e^{-jw\tau_1} + e^{-jw\tau_2} + e^{-jw\tau_3} + \ldots\} \quad (46)$$

where: $g(w)$ = the spectrum for a single dip/peak.

τ_i = time between initial dip/peak and the ith dip/peak

REFERENCES

[1] Amnon Yariv, "Coupled mode theory for guided wave optics," IEEE J. QE-9, p. 919-933, Sept. 1973.

[2] J.A. Bucaro, A. Dandridge, G.H. Sigel, Jr., J.H. Cole, S.C. Rashleigh, R.G. Priest, "Optical fiber sensor technology," , IEEE J. QE-18, p. 626-65, April 82.

[3] C.M. Davis, "Fiber optic sensors: an overview," Opt Eng, Vol. 24, p. 347-51, Mr/Apr 85.

[4] H. Suda, S. Shibata, M. Nak,"Double flame VAD process for high-rate optical preform fabrication," Electron Lett, Vol 21, p 29-30, Jan. 3, 1985.

[5] H.T. Shang, T.A. Lenahan, P.F. Glodis, D. Kalish, " Design and fabrication of dispersion-shifted depressed-clad triangular-profile (DDT) single-mode fiber," Electron Lett, Vol. 21, p 201-203, February 28, 1985.

[6] Bergh, Kotler, Shaw "Single-mode fiber optic directional coupler," Electron Lett, Vol. 16, p 260-61, March 27 1980.

[7] Hall, Yu,"Low loss fiber optic directional coupler," SPIE, Vol 478: Fiber Optic and Laser Sensors II, p 75-79, 1984.

[8] Stokes, Chodorow, Shaw, "All-single-mode fiber resonator," Optics Lett, Vol 7, p 288-90, June 1982.

[9] Hall, Yu, "Low loss fiber ring resonator," SPIE Vol 478: Fiber Optic and Laser Sensors II, p 104-108, 1984.

[10] S.A. Newton, J.E. Bowers, H.J. Shaw, "Single mode fiber recirculating delay line," SPIE Vol 326: Fiber Optics-Technology '82, p 108-15, 1982.

[11] M. Tur, J.W. Goodman, B. Moslehi, J.E. Bowers, H.J. Shaw, "Fiber optic signal processor with applications to matrix-vector multiplication and lattice filtering," Optics Lett, Vol 7, p 463-65, Sept 1982.

[12] B. Culshaw, "Optical fibre signal processing," SPIE Vol 468: Fibre Optics '84, p 167-73, 1984.

[13] K.P. Jackson, S.A. Newton, B. Moslehi, M. Tur, C.C. Cutler, J.W. Goodman, H.J. Shaw, "Optical fiber delay-line signal processing," *IEEE Trans Microwave Theory Tech*, Vol MTT-33, p 193-210, Mar. 1985.

[14] Zarinetchi, Meyer, Sanders, Ezekiel, "Passive resonator gyroscope," SPIE Vol 478: Fiber Optic and Laser Sensors II, p 122-26, 1984.

[15] T.Y. Hsu, V.J. TeKippe, "A passive fiber optic gyroscope," SPIE Vol. 478: Fiber Optic and Laser Sensors II, p 128-135, 1984.

[16] M.D. Rourke, "Measurement of the insertion loss of a single microbend," Optics Lett, Vol. 6, p 440-42, Sept. 1981.

[17] D.C. Marvin, N.A. Ives, "Wide-range fiber-optic strain sensor," Appl Optics, Vol 23, p 4212-4217, Dec. 1984.

[18] J.N. Fields, J.H. Cole, "Fiber microbend acoustic sensor," Appl Optics, Vol 19, p. 3265-3267, Oct. 1980.

[19] A.B. Tveten, A. Dandridge, C.M. Davis, T.G. Giallorenzi, "Fiber optic accelerometer," Electron Lett, Vol. 16, p 854-55, Oct. 1980.

[20] S.C. Rashleigh, "Magnetic field sensing with a single-mode fiber," Optics Lett, Vol. 6, p 19-21, Jan. 1981.

[21] W.B. Spillman, Jr., "Multimode fiber-optic hydrophone based on a schlieren technique," Appl Optics, Vol. 20, p 465-70, Feb. 1981.

END

DTIC

5-86